Geophysical Prospecting | **EAGE** EUROPEAN ASSOCIATION OF GEOSCIENTISTS & ENGINEERS

ORIGINAL ARTICLE

Imaging CO$_2$ reinjection into basalts at the CarbFix2 reinjection reservoir (Hellisheiði, Iceland) with body-wave seismic interferometry

S. H. W. Hassing[1] ◉ | **Deyan Draganov**[1] | **Martijn Janssen**[1] | **Auke Barnhoorn**[1] | **K.-H. A. A. Wolf**[1] | **Jens van den Berg**[1] | **Marc Friebel**[1] | **Gijs van Otten**[2] | **Flavio Poletto**[3] | **Cinzia Bellezza**[3] ◉ | **Erika Barison**[3] | **Baldur Brynjarsson**[4] | **Vala Hjörleifsdóttir**[4] | **Anne Obermann**[5] ◉ | **Pilar Sánchez-Pastor**[5] | **Sevket Durucan**[6]

[1]Delft University of Technology, Delft, Zuid-Holland, The Netherlands

[2]Seismic Mechatronics, Veldhoven, Noord-Brabant, The Netherlands

[3]Istituto Nazionale di Oceanografia e di Geofisica Sperimentale - OGS, Sgonico, Trieste, Italy

[4]Orkuveita Reykjavíkur, Reykjavík, Iceland

[5]ETH Zürich, Swiss Seismological Service, Zürich, Switzerland

[6]Royal School of Mines, Imperial College London, London, UK

Correspondence
S.H.W. Hassing, Delft University of Technology, Delft, Zuid-Holland, 2628CD, The Netherlands.
Email: s.h.w.hassing@tudelft.nl

Abstract

As part of the Synergetic Utilisation of CO$_2$ storage Coupled with geothermal EnErgy Deployment project, investigating CO$_2$ reinjection with different seismic methods, both passive and active seismic surveys have been conducted at the geothermal power plant at Hellisheiði, Iceland. During the 2021 survey, two geophone lines recorded noise for a week. We process the passive-source data with seismic interferometry to image the subsurface structure around the CarbFix2 reinjection reservoir. To improve image quality, we perform an illumination analysis to select only noise panels dominated by body-wave energy. The results show that most noise panels are dominated by air-wave energy arriving from the direction of the power plant. We use panels with a near-vertical incidence to create a zero-offset image and a larger selection of body-wave-dominated panels to create virtual common-shot gathers. We process the gathers with a simple reflection seismology processing workflow to obtain stacked images. The zero-offset images show a relatively lower signal-to-noise ratio and only horizontal reflectors. The stacked images show slightly dipping reflectors and possibly lateral amplitude variations around the expected injection region. This could indicate a region of interest for future research into the reinjection reservoir.

KEYWORDS
CO$_2$ sequestration, CO$_2$ reinjection, Hellisheiði, Iceland, Imaging, Passive method, Seismics, Monitoring, Seismic Interferometry

INTRODUCTION

The reduction of greenhouse gas emissions is one of the most important factors in mitigating the effects of climate change (Masson-Delmotte et al., 2018). Carbon capture and storage (CCS) has the possibility to be an important mitigation method (Aminu et al., 2017; Metz et al., 2005).

Geological carbon storage methods inject CO_2 into deep saline environments or depleted petroleum reservoirs as a supercritical fluid (Matter et al., 2016). As supercritical CO_2 is buoyant with respect to formation water at the relevant reservoir conditions, there is a risk of undesired leakage to other geological formations or the surface. There are different trapping mechanisms to keep the CO_2 underground, but it can take thousands of years for the majority of the CO_2 to be stored with the more stable trapping mechanisms (solubility and mineral trapping) (Metz et al., 2005).

The CarbFix project was started in 2006 to test a geological carbon storage method in basalts (Matter et al., 2011). This project improved the storage security of injected CO_2 by injecting CO_2 already dissolved in water into the formations (Sigfússon et al., 2015) and by injecting it into fresh basalts.

Injecting CO_2 dissolved in water means that solubility trapping is the starting condition after injection. Fresh basalts can dissolve to provide divalent cations that react with the CO_2 to form carbonate minerals (Matter et al., 2011), while little competing secondary mineralization has filled the pore space (Snæbjörnsdóttir et al., 2014). To test the method, a pilot project was set up at the Hellisheiði geothermal power plant in Iceland in 2012, where there was a supply of CO_2 to inject and there were fresh basalts in the subsurface.

The result of the pilot run was that more than 95% of the injected CO_2 was mineralized within 2 years after the injection started (Matter et al., 2016). After this success, the project was expanded with another reinjection site at Hellisheiði in the CarbFix2 project where reinjection started in 2014 (Sigfússon et al., 2015). This second field has become the major reinjection site at Hellisheiði.

The Synergetic Utilisation of CO_2 storage Coupled with geothermal EnErgy Deployment (SUCCEED) project aims to show that CO_2 reinjection increases geothermal performance and how different seismic techniques can be used for monitoring injected CO_2 (Durucan et al., 2021). This is accompanied by seismic field campaigns in two locations. One location is at the CarbFix2 reinjection reservoir at Hellisheiði, and the other is at the Klzlldere geothermal power plant in Turkey.

For CCS projects that inject supercritical CO_2, seismic methods are important monitoring techniques. When CO_2 is injected as a separate phase compared to the formation fluid, the seismic impedance of the formation changes significantly and provides a sharp contrast with the unaffected formations. This is used to monitor different CO_2 injection projects around the world (Furre et al., 2017; Huang et al., 2018; Pevzner et al., 2020). These surveys often rely on the assumption that the velocity change is only caused by fluid substitution. However, CO_2 can react with or dissolve the host rock, causing changes in the seismic velocity of the bulk rock (Lumley, 2010; Sim & Adam, 2016).

At the CarbFix2 injection site, the CO_2 is already dissolved during the injection, meaning that the strong velocity contrast due to fluid substitution is lacking. Instead, the changes in seismic velocity caused by chemical reactions after the injection of CO_2 could be used for monitoring.

Research into changes in seismic velocity due to CO_2 injection in basalts is limited, especially when only including injection with CO_2 dissolved in water. Laboratory experiments have varying results showing both decreasing (Kanakiya et al., 2017; Roy et al., 2016) and increasing (Adam et al., 2011, 2013) seismic velocity after injection. The experiments suggest that there is significant variability based on rock composition and pore structure, but more data are needed for conclusive links. Kanakiya et al. (2017) concluded that for characterization of reservoirs, site-specific experiments are needed.

For the CarbFix2 injection site, there are laboratory experiments looking into the seismic-velocity characterization with varying depth (Janssen et al., 2020, 2022), which can be used for initial velocity characterization. It is worth noting that the shallow seismic velocities in these models were shifted significantly downwards (from 4000 to 1800 m/s). Additional results from acoustic laboratory experiments in a borehole simulator on a basalt sample show that more injection of CO_2 decreases reflection amplitude off internal fractures but not travel time through the sample. The amplitude decrease reduces with distance from the injection centre. The reduction in impedance differences associated with a decrease in reflection amplitude, without a change in seismic velocity suggests a decrease in bulk density.

Based on geochemical monitoring and modelling at the injection site in Hellisheiði, it is suggested that the host rock has dissolved and new fractures have formed close to the injection well. This is caused by undersaturation of the injected fluid in certain minerals compared to the reservoir fluid and changes in pressure and temperature from injected fluids, respectively (Clark et al., 2020). This would suggest a lowered seismic velocity and density close to the injection well. As both the laboratory experiments and the geochemical studies suggest a decrease in seismic impedance in the affected layers, this will be used henceforward.

Assuming a simple layercake model with the seismic velocity and density increasing downwards, a small decrease in acoustic impedance in a lower layer would result in a decrease in reflection amplitude. This can be used as a working hypothesis when studying the final images.

To test the monitoring capabilities of different seismic techniques in the field, two seismic surveys were conducted for

the SUCCEED project in Hellisheiði during July 2021 and June 2022. Active-source surveys were conducted during both years, while a passive-source survey was performed during the July 2021 survey.

The aim of this work is to process the passive seismic data recorded on the second geophone network during the July 2021 survey with seismic interferometry (SI) to image the CarbFix2 reinjection reservoir. Because the geophone network was not deployed in the second survey, the passively recorded data from the geophones cannot be used for monitoring. However, the processed results can provide structural information that is valuable for verification and further processing of data.

The CarbFix2 injection site at Hellisheiði

The Hellisheiði geothermal field is part of the Hengill volcanic system with the CarbFix2 injection site lying on the western flank of the Hengill volcano itself (Snæbjörnsdóttir et al., 2018). The Hengill volcanic system lies on the triple junction formed by different parts of the North American and Eurasian plate boundary on Iceland. These are two rift zones, the Reykjanes Peninsula Volcanic Zone and the Western Volcanic Zone, and the transform South Island Seismic Zone (Einarsson, 2008).

The volcano itself consists primarily of hyaloclastic formations and lava sequences (Gebrehiwot et al., 2010). The hyaloclastic formations form under ice caps during glacial periods and have a limited spatial extent. The lava sequences fill local depressions during interglacial periods (Snæbjörnsdóttir et al., 2018). This means local highs consist of hyaloclastic formations, while low-lying areas, such as the Hellisheiði area, are filled with successions of hyaloclastic formations and lava sequences.

Intrusions become more common from 500 m below sea level downwards (Snæbjörnsdóttir et al., 2018). Deeper than 1000–1300 m below sea level, a thermally altered lava sequence intersected by many intrusions can be found (Franzson et al., 2010; Ratouis et al., 2022). This layer originates from another nearby volcano and is considered the base of the Hengill volcano. The layer has been dated to 0,4 Ma, giving an upper bound to the age of the volcano (Franzson et al., 2010).

Two schematic geological sections from the model described by Poux et al. (2018) from directly under the survey area can be found in Figure 1. As the model only distinguishes between the lithologies lava sequence, hyaloclastite and intrusion and there is not a lot of specific information on this part of the area, the resulting sections are most likely simplistic. For example, there is no previous seismic information on the relevant scale of this area. The sections should not be seen as a definitive description of the area, but as giving an idea of what results could be seen.
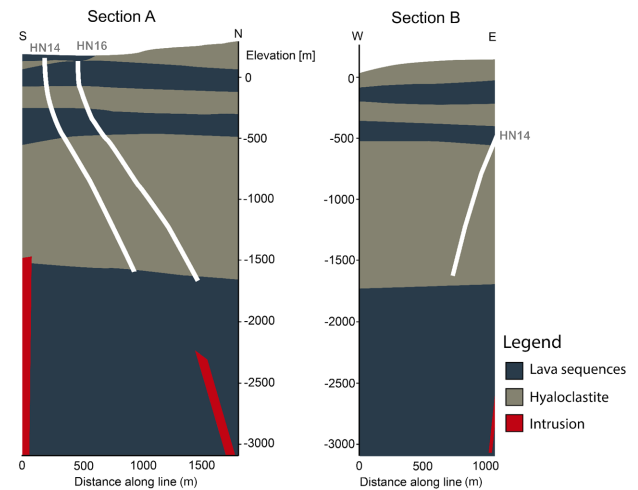

FIGURE 1 Schematic geological sections of the subsurface below the survey area. Exact locations of the lines are shown in Figure 2. The different lithologies are indicated in the legend. The intrusions show the vertical extent found in wells. Two injection well trajectories (HN14 and HN16) are projected onto the sections. Sections based on Poux et al. (2018).

The sections show an alternating pattern of hyaloclastic formations and lava flows until 500 m below sea level. The base of the Hengill volcano is found around 1600 m below sea level, and the injection wells reach down to this same level. The casing of injection wells HN14 and HN16 reaches down to 690 and 660 m below the surface, respectively (Clark et al., 2020).

The injection transport model in Ratouis et al. (2022) showed that the injected fluid sinks just after reinjection and can be found down to 2500 m below the surface under the reinjection well. Flow in the model happens towards the northeast. A map showing possible noise sources relative to the exact positions of the geophones is shown in Figure 2. The CO₂ air capture plant was under construction during the survey. This meant that there was both heavy traffic and construction work close to the southern part of the network. Power lines also cross over the geophone line in the same area.

The locations of the reinjection wells are also indicated in Figure 2. Two wells cut through the southern part of the main line. If there is an observable effect due to the CO₂ reinjection, it is expected to be observed in the southern half of the main line from the end of the casing around 660 m below the surface to the deepest fluid pathways at 2500 m below the surface.

Seismic interferometry

Seismic interferometry (SI) is originally based on the one-dimensional theory developed by Claerbout (1968) but has been expanded to three dimensions (Wapenaar et al., 2004). For an overview of the theory behind SI and the derivations
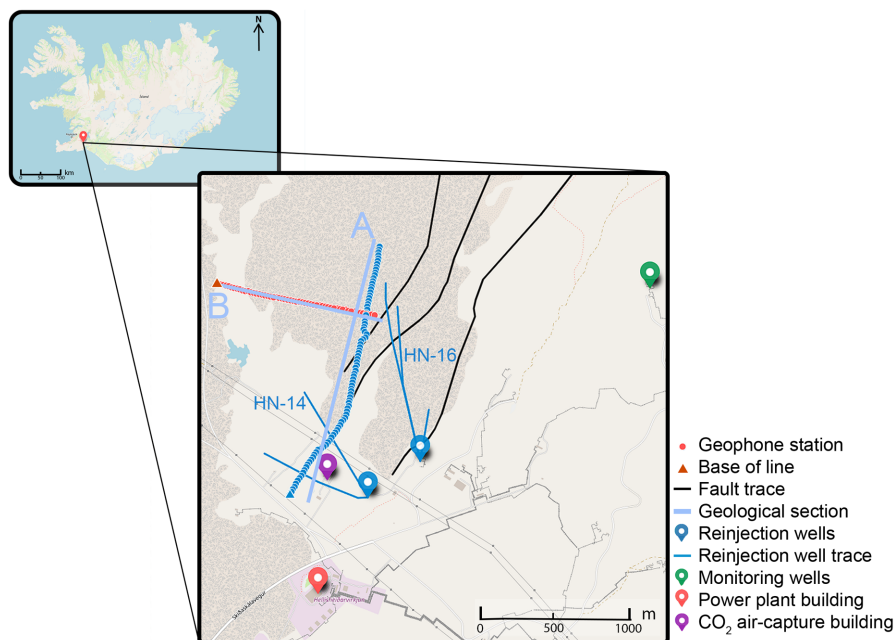
FIGURE 2 Map view showing the acquisition geometry of the survey at Hellisheiði. The main geophone line is indicated with blue circles, while the cross-line is indicated with red. The base of each line is shown as a small triangle. The light blue lines indicated with A and B show the locations of the two geological cross sections in Figure 1. The well and fault traces are based on Ratouis et al. (2022). Map from OpenStreetMap contributors under ODbL.

of its equations, see, for example, Wapenaar and Fokkema (2006) and Wapenaar et al. (2010).

SI allows a virtual response to be retrieved between two receivers by cross-correlating the two receiver recordings. The virtual response shows what would have been measured at the second receiver if the source was located at the first receiver location, assuming a lossless medium and no other active sources. Effectively, the method removes the shared path between two receivers from the recorded signal. This also means that the exact source position does not have to be determined.

To properly retrieve the seismic response, enough sources to effectively surround the receivers should be used and the result from the cross-correlation of the recordings from each source should be summed (Wapenaar & Fokkema, 2006). The exact amount of sources is not the most important factor. It is rather important that there are at least two sources per wavelength at the depth level of the source. When noise is used, instead of using separate recordings from each source, the continuous noise is cut into noise panels, each is cross-correlated and the results are summed. For noise sources, it is also not necessary that each noise source should be treated separately. Multiple noise sources can be active at the same time, as long as they are uncorrelated.

The principle of SI can be applied in many different configurations, both with active- or passive-source seismic data, with surface waves or body waves. When using passive seismic data, there needs to be some source for the

seismic events. Depending on the imaging target and recording time, global earthquakes (e.g., Ruigrok & Wapenaar, 2012; Andrés et al., 2019), local earthquakes (e.g., Nakata et al., 2014; Nishitsuji et al., 2016), microseismicity (e.g., Polychronopoulou et al., 2020; Kim et al., 2017) or ambient noise (e.g., Nakata et al., 2015; Olivier et al., 2015) can be used.

To image the reinjection reservoir in Hellisheiði, body-wave arrivals from local microseismicity provide the best option, due to the large amount of seismicity at depth. This provides sources that illuminate the target reservoir. We use P-waves, meaning that only the vertical component recorded on the geophones is used.

Applying SI to body-wave arrivals at the surface retrieves a reflection response from a virtual source at one receiver location. Using every trace, while keeping the virtual source position constant, results in a virtual common-source gather. A set of virtual common-source gathers can be processed with a standard reflection processing workflow to obtain a stacked image.

Using local microseismicity does require that enough seismic events occur during the recording time. More recorded events result in a higher quality of the final image. Luckily, the Hengill area is one of the most seismically active areas in Iceland. Between 1994 and 2007, 40% of the recorded earthquakes in Iceland were located there (Jakobsdóttir, 2008). This seismic activity was mostly caused by rifting and volcanic activity.

The geothermal production and the reinjection of CO$_2$ have also caused induced seismicity. Under the CarbFix2 injection site, two clusters of seismicity are found focused around depths of 2 and 5 km (Duran Neme, 2021; Obermann et al., 2022). These clusters are associated with induced and natural seismicity, respectively. The CarbFix2 injection site was found to be the most seismically active in the area with 27% of the local seismicity (Duran Neme, 2021). The presence of large amounts of seismicity underneath the imaging target gives confidence in the possibility of retrieving images of the reservoir after the utilization of SI.

A second major problem is that surface-wave energy dominates most noise panels, obscuring the body-wave arrivals. It is possible to try to filter out the surface-wave energy, but Draganov et al. (2010) showed that using only panels that are dominated by body-wave energy also results in a better image.

One method of distinguishing between body-wave and surface-wave dominated panels is by performing an illumination analysis on each panel (Panea et al., 2014). This finds the slowness of the dominant event in each panel. As surface waves are characterized by a relatively higher slowness than body waves, a limit can be set to discriminate between them.

A second advantage of this method is that it allows selecting only events with a near-vertical incidence. This means that a zero-offset section can directly be retrieved (e.g., Casas et al., 2019; Polychronopoulou et al., 2020). As the virtual source and receiver are colocated, each trace is only autocorrelated, simplifying the processing required for this image compared to the stacked image.

To get a better grip on the results we expect from the survey, we consider SI reflection surveys done in similar (volcanic) environments. To start, we introduce three surveys from Iceland.

On the Reykjanes peninsula, SI was applied to test for reflection information with a sparse geophone network (Verdel et al., 2016). Comparison with earthquake coda information shows a good agreement with the SI results. At the Krafla, SI reflection imaging of magma was done as part of the IMAGE project (Kim et al., 2017). Several reflectors (their Fig. 12) were imaged that could be associated with magma bodies in the subsurface. The same method was applied at Hverahlíð, close to Hellisheiði, to image the subsurface (Stoch, 2020). Various reflectors are visible in their Fig. 17/18 with a possible interpretation provided for three of them.

At the Planchón-Peteroa Volcanic Complex in Argentina/Chile, SI was applied to verify a subsurface model (Casas et al., 2019). Multiple contacts are found down to 4 km that fit with the model of the area. At the Los Humeros geothermal field in Mexico, SI with autocorrelations was used to find a relatively good correspondence with modelled data (Verdel et al., 2019).

In general, these studies show that the results have a low signal-to-noise ratio and reflectors can mostly be identified by their coherence over several traces. The frequency content, and thus the resolution, is generally low. The reflectors that are found generally correspond to the expected locations of reflectors found in the subsurface with other methods.

METHODS

The passive-source survey was recorded to accompany the main two active-source surveys. These surveys used a single buried, helically wound distributed acoustic sensing cable and an electrical seismic vibrator source. During the 2021 survey, two geophone networks were also present. These geophone lines recorded the active-source survey and recorded passively for about 9 days.

The geophone network consisted of 148 three-component 2-Hz geophones with 20 m spacing spread over two lines. The main line (92 geophones) was oriented about south-to-north, while the cross-line (56 geophones) was oriented about west-to-east. Their exact positions can be seen in Figure 2. More details and intermediate results of the survey are presented in Stork et al. (2022) and Bellezza et al. (submitted).

The full processing workflow for this work is summarized in Figure 3. The code used to process the data is written in Python 3.9.12 and built upon ObsPy (Beyreuther et al., 2010; Krischer et al., 2015). It can be found at https://github.com/shwhassing/thesis_functions.

The passive seismic data were recorded from 21 July to 30 July 2021. Only the times when all stations were active are used in the processing, meaning that around 140 hours of data are available.

The passive seismic data are split up into noise panels of 10 s, providing a total of 50,506 noise panels. This panel length is chosen so that the final images include the deepest level at which injected fluid is expected in the reservoir (around 2500 m below the surface) and two surface multiples of the possible reflection from that level. This rough calculation is done with the lowest P-wave velocity of 1800 m/s based on laboratory experiments on samples from the area (Janssen et al., 2022).

It is possible to include an overlap of the noise panels. This would improve the granularity of the data and likely provide more body-wave dominated panels from the illumination analysis, but it would also increase the computational load. Because a large amount of panels is available already, no overlap is used.

Before the illumination analysis, each trace in each panel is normalized and a frequency filter is applied to the data. The normalization is done by dividing the traces by their root-mean-square amplitude to remove amplitude differences due to different sources or measuring instruments. The frequency filter is used to remove clear sources of non-body-wave
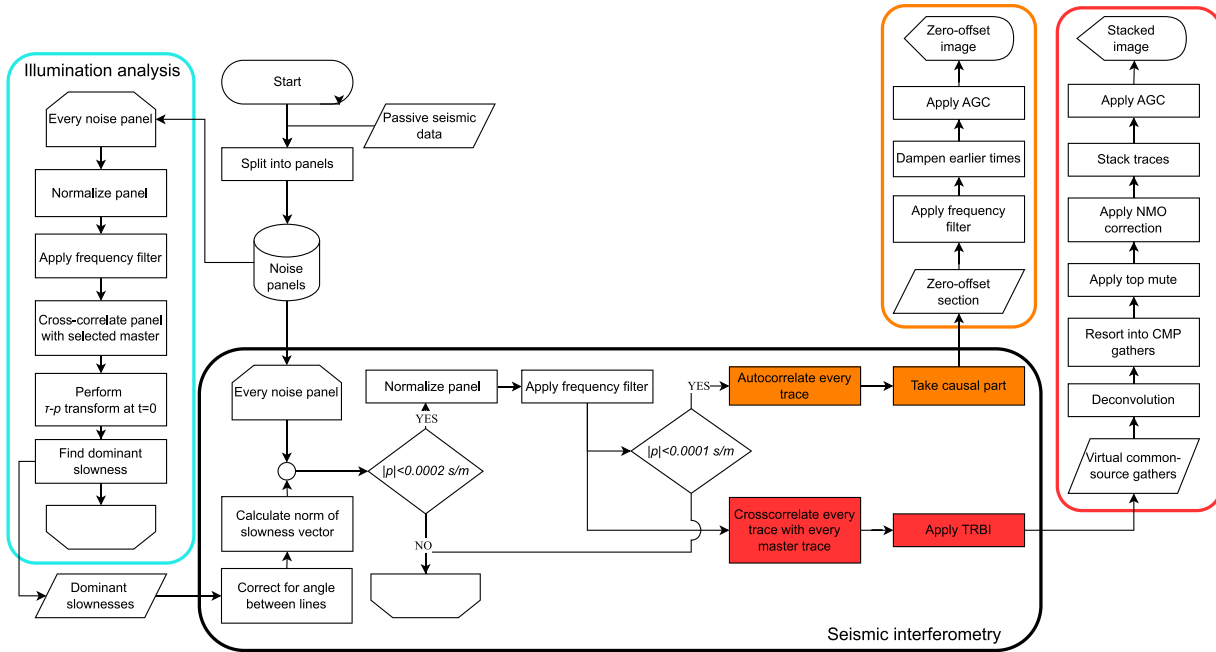
FIGURE 3 Flowchart showing the different steps used to create seismic images from the raw data. The blue box shows the steps taken during the illumination analysis. The resulting dominant slowness for each panel, for each line is saved. During the seismic interferometry, those panels that fit the criterion for cross-correlation are used to create virtual common-source gathers. Those that fit the stricter criterion for autocorrelation are used to obtain the zero-offset section. The specific paths leading to the zero-offset image and the stacked image are denoted in orange and red, respectively. TRBI, time reversal before integration; CMP, common midpoint; AGC, automatic gain control; NMO, normal moveout. These terms are expanded upon in the main text.

energy. Initially, this is a simple notch filter, based on visual inspection of the data and the amplitude spectrum. This filter is revisited after the first results have been generated.

The illumination analysis is based on the method used in Almagro Vidal et al. (2011) (see also Almagro Vidal et al., 2014). This technique applies a τ-p transform to each cross-correlated panel at $t = 0$. The events that pass through time zero show the illumination characteristics of the noise sources. As the illumination analysis is independent between stations (Almagro Vidal et al., 2014), the illumination analysis is performed at a single station at the crossing of the two lines to save computation time.

The τ-p transform allows the identification of the slowness of the dominant event in the panel. As the cross-correlated panel contains both a causal and an acausal part, both negative and positive slowness values are evaluated. The sign of the slowness indicates the illumination direction and is relevant later in the process.

Evaluating the slowness using a single geophone line gives ambiguous results. Surface-wave events that propagate in a direction perpendicular to the line are also characterized by a low slowness. Instead, the illumination analysis is performed on both lines separately. The separate measurements are interpreted as two measurements of the slowness vector along the surface. The length of the slowness vector is calculated by first correcting for the angle between the geophone lines and

then taking the norm of the resulting values. When the resulting length of the dominant slowness vector is low enough, a body-wave event is recognized.

Two examples of noise panels, together with the average amplitude spectrum of both non-body-wave panels and body-wave panels, are shown in Figure 4. The amplitude spectra show that the selected body-wave-dominated panels contain higher frequencies.

Panels with dominant slowness vector norm below 0.0002 s/m are used to create the virtual common-source gathers. The zero-offset section requires a stricter selection criterion to only include events with a nearly vertical incidence. Thus, only panels with a dominant slowness vector norm below 0.0001 s/m are used. The selected panels are first normalized, and the selected frequency filter is applied.

After correlation, the causal, acausal or both parts of the resulting traces must be selected. For the autocorrelated traces, the causal part is taken. For the cross-correlated traces, a process called time reversal before integration is used, first applied by Ruigrok et al. (2010). This method takes the acausal or causal part of a single trace based on its location relative to the virtual-source location and the sign of the dominant slowness found by the illumination analysis.

The retrieved traces from each selected panel are summed for each receiver position to obtain the zero-offset
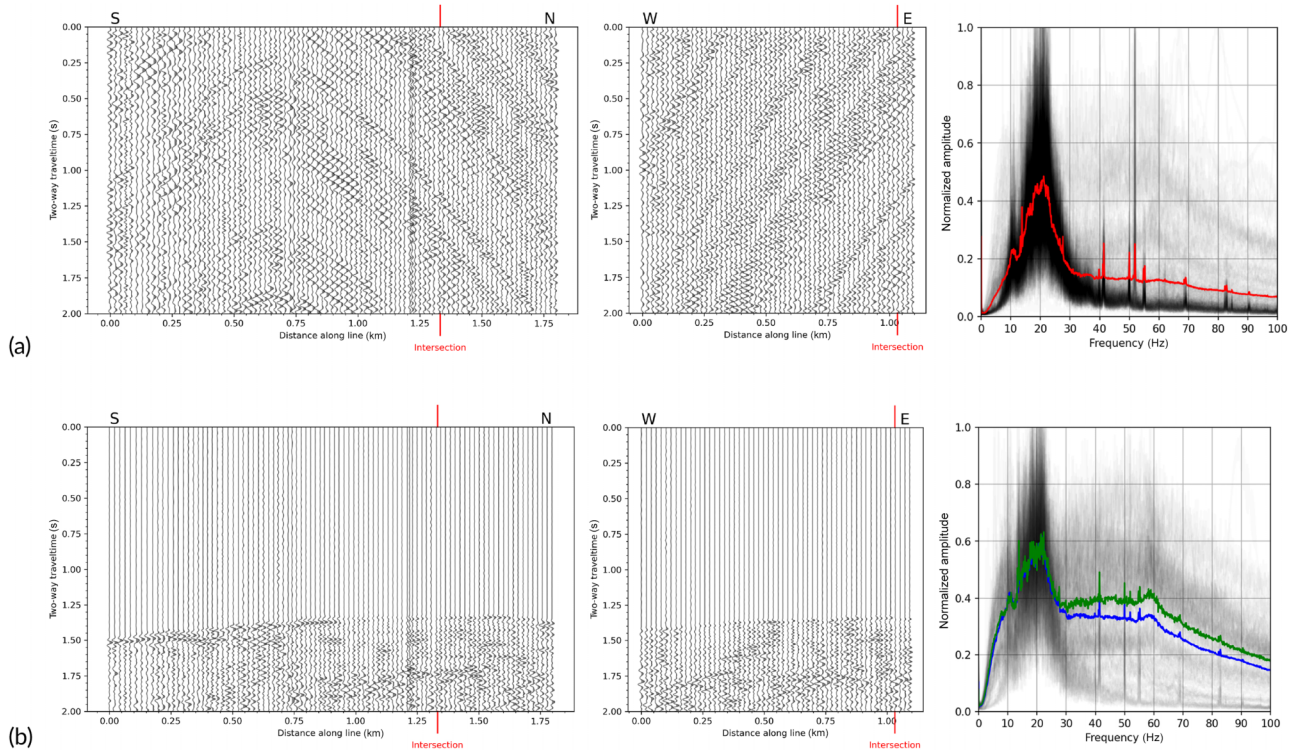
FIGURE 4 Two examples of noise panels (a) not dominated by body waves and (b) dominated by body waves recorded along the main line (left) and along the cross-line (middle). A Butterworth bandpass filter with cut-off frequencies at 5 and 40 Hz is applied to the wiggle plots for visual purposes. (right) Unfiltered amplitude spectra of (a) 200 randomly selected panels not dominated by body waves (grey) and their average (red) and (b) all panels selected with the selection criteria described in the text, where the blue line shows the average of the panels with a dominant slowness vector norm below 0.0002 s/m, while the green line shows the average below 0.0001 s/m. Note that the individual spectra of the panels not dominated by body waves are normalized to their maxima for visualization purposes.

section from the autocorrelated traces and the virtual common-source gathers from the cross-correlated traces. The zero-offset section is processed with simple image-processing steps to obtain the final zero-offset image (Figure 3). A band-pass filter is manually designed based on the image. This is applied retroactively before the illumination analysis to obtain an improved image. The bandpass filter is implemented as a Butterworth filter of order 4 with cut-off frequencies of 5 and 40 Hz. The first 100 ms are dampened to remove the large spike at $t = 0$ that would otherwise dominate the image. Finally, automatic gain control is applied to balance amplitudes through the image.

The retrieved virtual common-source gathers are processed further with a basic reflection processing workflow (Figure 3) after a Wiener deconvolution. The common midpoint gath-ers are prepared for the normal moveout (NMO) correction by applying a top mute. Because of the limited offset in the geophone lines and the quality of the data, velocity picks are difficult. For this reason, a single velocity function with five velocity picks (Table 1), based on the data and the labora-tory information from Janssen et al. (2022), is used for the NMO correction.

TABLE 1 Root-mean-square velocity picks used to create the velocity model used for the normal moveout correction. Values between the picks are linearly interpolated. A single velocity function is used for both sections..

Time (s)	Velocity (m/s)
0.0	1800
0.35	2200
0.5	2500
1.1	4000
2.0	6000

RESULTS

Figure 5 shows how the results of the illumination analysis with the bandpass filter applied beforehand vary over time. The most prominent feature is a continuous band of similar slowness values around 0.0029 s/m. The associated apparent velocity of 345 m/s would suggest that these panels are dominated by air-wave noise. This pattern is broken in a zone demarcated by vertical purple lines. This zone contains a
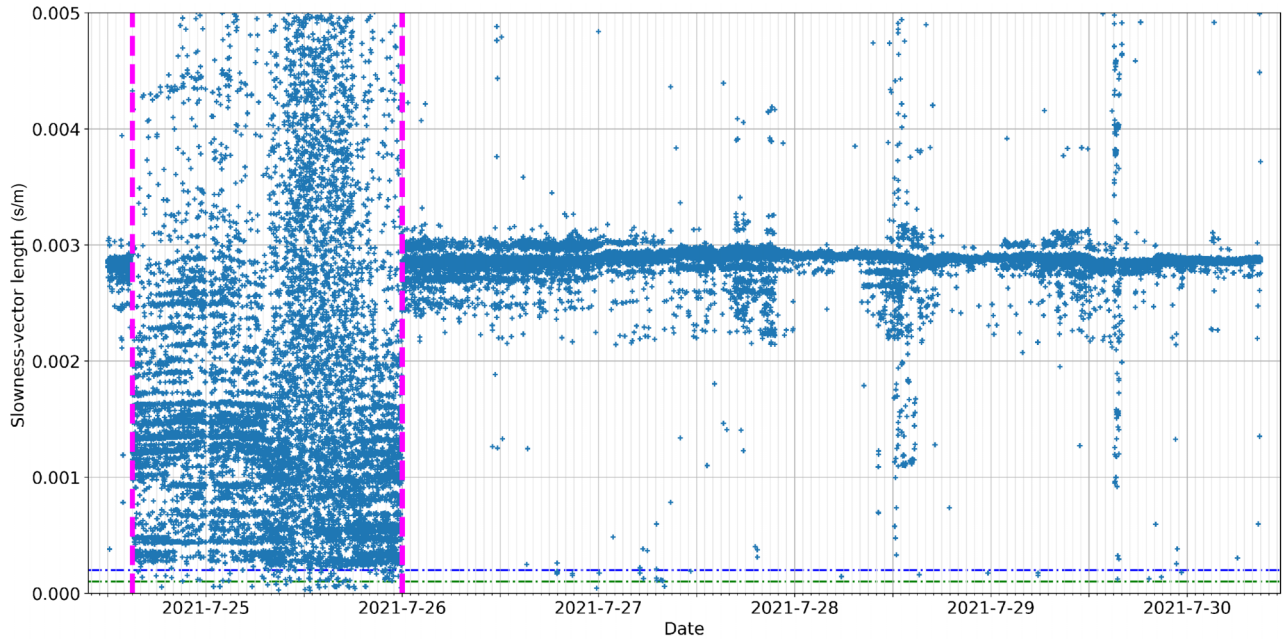
FIGURE 5 Results of the illumination analysis as the length of the slowness vector plotted through time. Every marker indicates the dominant slowness of a single noise panel by using the results from each geophone line as a vector element. The figure shows a clear horizontal band around 0.0029 s/m. This pattern is broken up in the area between the vertical purple lines, where a larger spread in slowness values can be found. Horizontal blue and green dash-dotted lines indicate the selection criteria for panels in creating the stacked and zero-offset images, respectively.
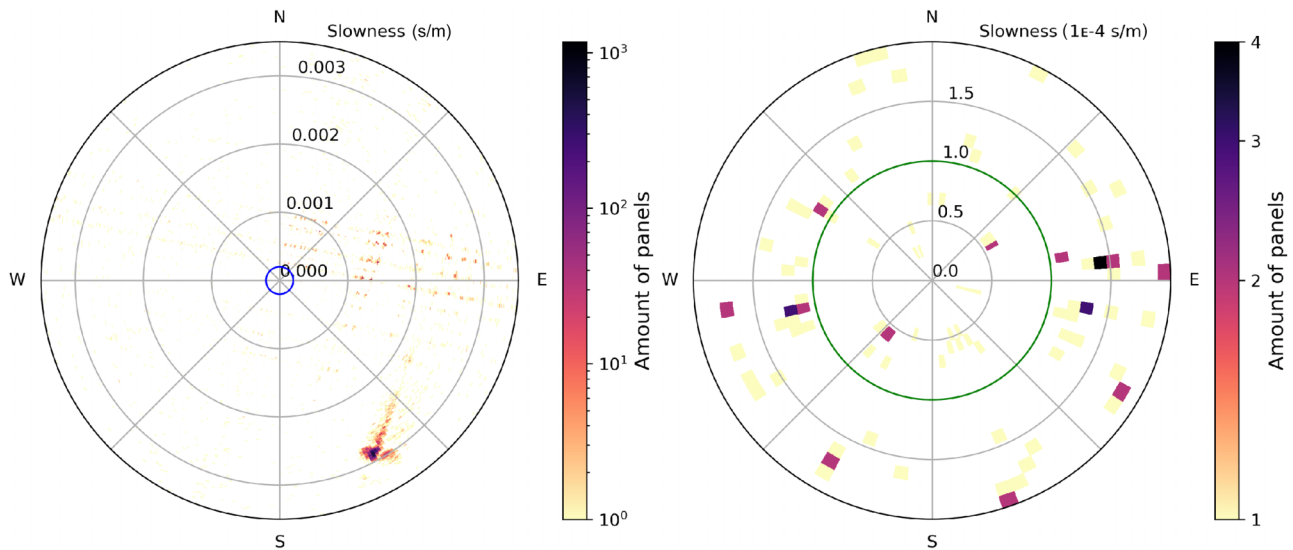

FIGURE 6 A two-dimensional histogram showing the results of the illumination analysis varying with back azimuth. The blue circle in the left window indicates the criteria used to select panels for the virtual common-source gathers. This area is shown enlarged in the right window. The green circle in the right window shows the criteria used to select panels for the zero-offset section. Note that the scale of the amount of panels is logarithmic. The plot shows that the large majority of noise panels are dominated by events arriving from the southeast.

larger spread in dominant slowness values and smaller bands of similar slowness values. The most likely explanation is a heavy storm that passed over the field area during the 2-day interval.

Similar large spreads of slowness values can be found around noon on the 28th and 29th of July. These spreads are associated with noise from the active-source campaign close to the evaluation station of the illumination analysis. The

figure shows that the large majority of panels do not fulfill the selection criteria we chose for SI.

This is illustrated further in Figure 6. Here, the directionality of the retrieved slowness vectors is used. As the vector points in the direction of propagation, the direction the events are coming from is the reversed vector. The vector orientation can be converted to back azimuth to show this. The length of the vector is indicated by the distance from the centre of the plot. The back azimuth and vector length are taken together to plot a polar histogram and show where the dominant events in most panels originate from.

The large majority of noise panels are characterized by a back azimuth from the southeast and a high slowness. This is also the direction of the main part of the power plant. There is also a smaller spread of peaks towards the northeast. These are noise panels taken from the chaotic zone in Figure 5. The enlarged window shows that the selected panels show a roughly equal spread over the selected area.

In total, 131 panels are selected to retrieve the virtual common-source gathers, while 36 are selected to retrieve the zero-offset section. Although the slowness of the total group of noise panels is highly clustered, the selected noise panels show a good spread over both back azimuth and slowness. As discussed, this spread of sources is a requirement for seismic interferometry (SI) to provide useful results. The amount of panels is relatively small compared to the total amount of noise panels, but that amount can still be sufficient for the retrieval of reliable SI results. The most likely explanation for the relatively small amount is the high level of noise from both the wind and the power plant.

In total, the two figures show that most noise panels are dominated by continuous noise from a small group of sources. At some intervals, this noise is overpowered by other sources of noise, that is, a storm or human activity close to the receiver.

The final zero-offset and stacked images along the main line and cross-line are shown in Figures 7 and 8, respectively. A tentative time-to-depth conversion based on the velocity model and averaged reflector depths is added on the right axes. Considering the difficulties with velocity picks mentioned before, these depths cannot be used for final interpretations. They can, however, lend some extra information when used in conjunction with other evidence.

The zero-offset image shows multiple clear, horizontal reflectors. At shorter traveltimes, down to the red arrow at 0.55 s two-way traveltime (TWT), multiple prominent low-frequency horizontal reflectors are found. At longer traveltimes, the images are very noisy and reflectors become more difficult to track. Nevertheless, there are multiple other reflectors to find. Two of these are indicated with green and blue arrows.

The stacked image exhibits more continuous reflectors and overall appears less noisy. Similar horizontal, strong reflec-

tors are shown above the red arrow. In the middle of the line, these horizontal reflectors are disturbed and broken up under the cyan line. Between the red and green arrows, the reflectors are more difficult to track through the centre of the main line section but appear horizontal. On the cross-line, these same reflectors appear horizontal, except the ones closest to the green arrow (one of which is indicated by a green line), where an antiform appears at the centre of the line. Below the green arrow, the reflectors clearly dip towards the south and east. The most prominent reflectors correspond between the zero-offset and stacked images, but the dipping reflectors are only found on the stacked images.

The stack resulting from the active-source campaign is shown in Figure 9. A bandpass filter between 4–8–12–16 Hz is applied to this stack to make the comparison with the images from the passive-source data easier. Despite this, the resolution of the active-source stack image is higher than in the passive-source stack.

As can be seen in the comparison in Figure 9b, the reflectors in the two images generally line up above 0.5 s TWT. Below 0.5 s TWT, the active-source stack shows more local variation and undulating surfaces, while the passive-source stack shows strictly horizontal layers. These general observations from the different resulting images correspond well to the theory that was used to generate them. The zero-offset image shows more detail as only the subsurface under a station is sampled. This results in a final image with more reflectors, but a lower signal-to-noise ratio. As only (nearly) vertically travelling events are selected, dipping reflectors cannot be imaged.

The stacked image combines the traces at different offsets with a set midpoint. As a result, the reflectors on the stacked image are slightly smeared out but the signal-to-noise ratio is higher. Using more offsets also allows for dipping reflectors to be imaged. The higher resolution recorded in the stacked section from the active-source campaign can be obtained because the source function is controlled and has a higher frequency content.

Compared to the other SI reflection studies mentioned in the Introduction, both types of sections show a large amount of recovered reflectors and a relatively high resolution. Based on the general knowledge of the seismic velocities of the subsurface in the area, reflectors are recovered deep enough to image the full injection reservoir.

INTERPRETATION AND DISCUSSION

In the results of this survey, both the main and cross-line show multiple, horizontal, clearly defined reflectors visible down to 0.55 s two-way traveltime (TWT, indicated by the red arrows). Considering the schematic nature of the geological
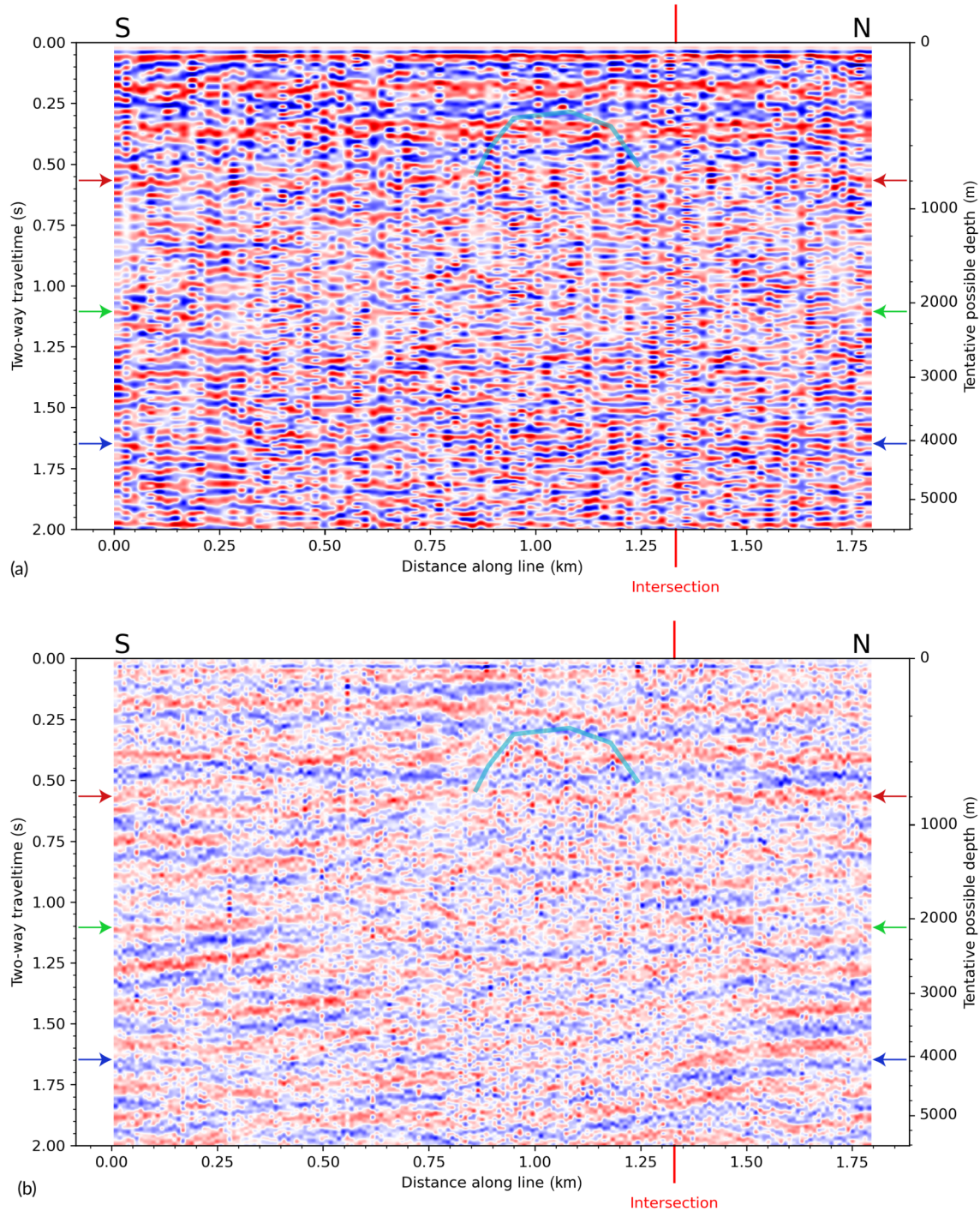
FIGURE 7 The zero-offset image (a) and stacked image (b) for the main line, capped at 2.0 s two-way traveltime. Automatic gain control with a window length of 1.0 s has been applied to both images before plotting. Blue indicates negative amplitudes, while red indicates positive ones. The intersection with the cross-line is indicated with red lines outside of the axes. The zero-offset image is noisier and shows primarily horizontal reflectors. A tentative first time-to-depth conversion based on the velocity model is shown along the right axis. The stacked image shows more continuous and dipping reflectors. Dipping reflectors show up from 0.7 s two-way traveltime downwards.

sections discussed above and shown in Figure 1, the imaging results from seismic interferometry suggest that the shallowest part of the sections contain layers with more frequent alternations between different lithologies than what is suggested by the limited knowledge in the geological sections.

The depth information supports that this zone with frequent alternations shown in the seismic images (down to 700–800 m depth) corresponds to the zone with multiple alternations shown in the geological sections (down to roughly 600–700 m depth).
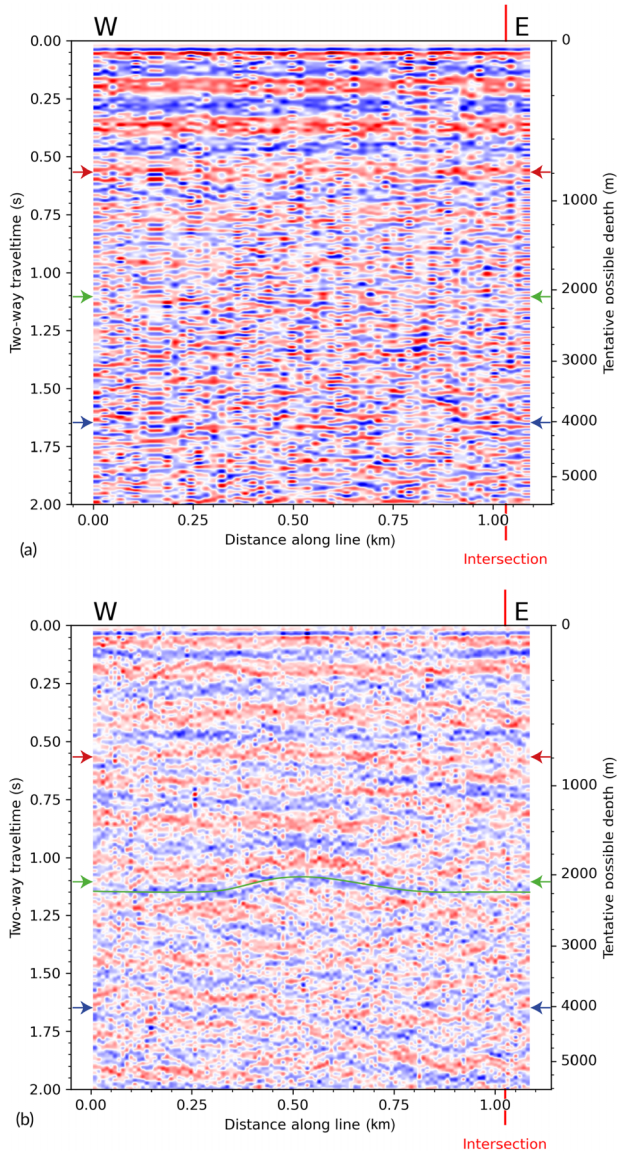
FIGURE 8 The zero-offset image (a) and stacked image (b) for the cross-line, capped at 2.0 s two-way traveltime. The intersection with the main line is indicated with red lines outside of the axes. A large circular anomaly is visible around 0.25 s two-way traveltime and 450 m along the line on the zero-offset section, while it is not visible on the stacked section.

The base of the Hengill volcano is more difficult to find. The reflector indicated by the green arrow shows a change from horizontal to dipping structures. It could be that the dipping reflectors are the older, alternated layers from another volcano and this reflector forms the base of the Hengill volcano. Based on the depth information, this reflector is found slightly too deep, but this might also be caused by the unreliable depth information.

Using these boundaries, the injected CO$_2$ would be imaged between 0.55 and 1.10 s TWT, while the injected fluid would

sink even deeper after injection. In the area marked with the cyan line along the main line, the amplitude of the reflectors is lower than at similar traveltimes along the line and the reflectors are less continuous. This reduction in amplitude could be caused by the injected fluid, as we hypothesized in the Introduction. The effect stretches downward from the marked area, but a lower boundary is difficult to mark. A slight decrease in amplitude is found in the active-source image, as well, but this can also be observed elsewhere in the image.

If clear changes could be found in follow-up surveys in the same area, this effect could be used as a starting point for further research into the reinjection site.

Note that the passive-source data might contain surface-related multiples. Such multiples would also be present in the active-soruce data, though, which means that the conclusions from the comparison of the results of the two data types do not change.

During the processing and the plotting, different amplitude corrections were performed on the data. The panel normalized applied before correlation is applied equally to the whole panel to eliminate the influence of the absolute strength of the recorded events. This is a necessary step to retrieve a correct final image. Automatic gain control is used before plotting the images. A window length of 1.0 s is used so that relative amplitude variations can still be identified. This also lowers the effect on lateral changes in amplitudes. To be able to draw meaningful conclusions, more data should be gathered in the area. Follow-up surveys, with, for example, longer passive-source recordings can be compared to find changes in the images. A survey using a longer survey line would be able to build an accurate velocity model that could also be applied retroactively. If borehole seismic methods are used in the area in the future, this could provide a large increase in the quality of the velocity model. Without further information on the subsurface, the results of this survey are difficult to verify; nevertheless, these results provide a starting point to seismically interpret the subsurface of the Carbfix2 reinjection reservoir.

The processing workflow used in this work could also be adapted to automatically process passive-source data coming in from the field. A master station, noise panel length and a sufficient frequency filter to apply to the data should then be decided upon, but no further human input would need to be given. The incoming data can be split up into panels and the illumination analysis done on the go. This would indicate how many noise panels are useful for further processing.

With a maximum slowness set, the selected noise panels can even be processed into a 'progress' zero-offset image. This gives an intermediate view of the results of the passive-source survey during recording.
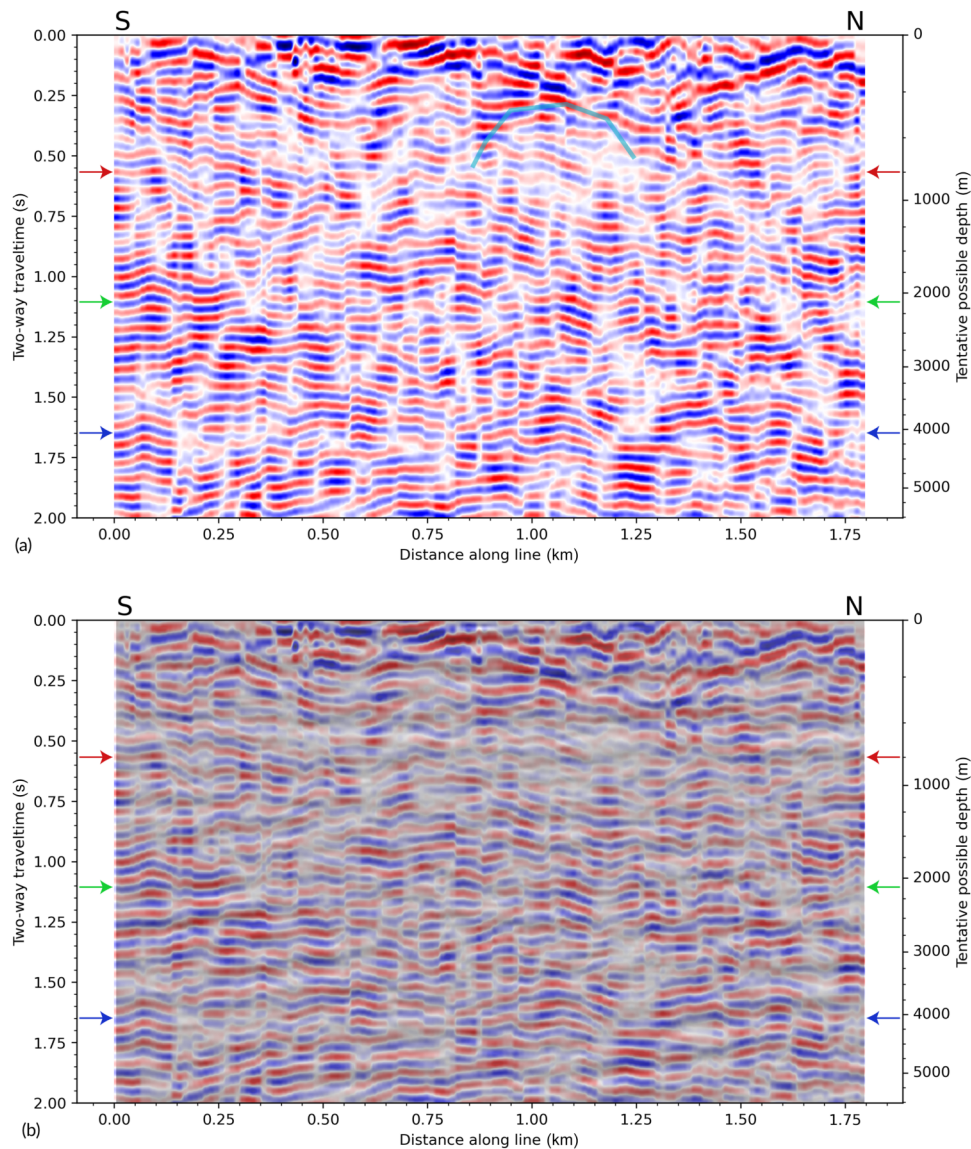
FIGURE 9 (a) A stacked section based on the active data with gain applied after stacking. A bandpass filter at 4–8–12–16 Hz has been applied for a better comparison with the passive data. The same window automatic gain control length of 1.0 s as in Figures 7 and 8 has been applied. When comparing the images, it is important to consider that in the processing of the passive data, the data are zero phase, while the active data are mixed phase. This means that the peak amplitude from the same reflection will be slightly shifted between the two images. (b) A comparison of the stacked sections with the passive-source data (white to black, see also Figure 7b) in the background and the active source data (blue to red) in the foreground. An additional Gaussian blur with a standard deviation of 1.2 (where 1.0 is the distance between data entries) has been applied to the passive-source data for easier comparison.

CONCLUSIONS

We recorded passive seismic data along two perpendicular lines (main and cross-line) above the CO_2 reinjection site of Húsmúli of the CarbFix2 project at Hellisheiði, Iceland. We processed these data using body-wave seismic interferometry to image subsurface structures including the reinjection reservoir. We applied an illumination analysis to estimate the slowness of the dominant event in each panel of noise, allowing us to use only panels dominated by body-wave noise and exclude panels that are dominated by surface-wave noise for the retrieval of final seismic-interferometry results. This resulted in a zero-offset image and a stacked image for both the main line and the cross-line.

The illumination analysis showed that the great majority of noise panels are dominated by noise characterized by an apparent velocity corresponding to the velocity of sound coming from the direction of the Hellisheiði power plant. The final images show some geological features that appear to correspond to the schematic geological model available for the area.

Down to 0.55 s two-way traveltime, horizontal reflectors are found below both lines. Dipping reflectors are found below 1.1 s two-way traveltime. We theorized that this could represent the base of the Hengill volcano. A comparison at lower frequencies between the active-source stack, recorded along the main line, and the passive-source stack shows that there is an agreement between the two images at those frequencies.

We speculated that some effects of the CO$_2$ reinjection might be visible on the main line images. However, without other monitoring seismic surveys to compare the image with, this cannot be concluded with certainty.

DATA AVAILABILITY STATEMENT
The data used in this work can be provided by contacting the correspondence address and after approval of all relevant partners.

ORCID
S. H. W. Hassing https://orcid.org/0009-0005-7323-1971
Cinzia Bellezza https://orcid.org/0000-0001-8347-8138
Anne Obermann https://orcid.org/0000-0001-6933-6301

REFERENCES
Adam, L., Otheim, T., van Wijk, K., Batzle, M., McLing, T.L. & Podgorney, R.K. (2011) CO$_2$ sequestration in basalt: carbonate mineralization and fluid substitution. In: *SEG technical program expanded abstracts 2011* Houston, TX: Society of Exploration Geophysicists, pp. 2108–2113.

Adam, L., van Wijk, K., Otheim, T. & Batzle, M. (2013) Changes in elastic wave velocity and rock microstructure due to basalt-CO$_2$-water reactions. *Journal of Geophysical Research: Solid Earth*, 118(8), 4039–4047.

Almagro Vidal, C., Draganov, D., van der Neut, J., Drijkoningen, G. & Wapenaar, K. (2014) Retrieval of reflections from ambient noise using illumination diagnosis. *Geophysical Journal International*, 198(3), 1572–1584.

Almagro Vidal, C., van der Neut, J., Draganov, D., Drijkoningen, G. & Wapenaar, K. (2011) Retrieval of reflections from ambient-noise field data using illumination diagnostics. In: *2011 SEG annual meeting*. Houston, TX: Society of Exploration Geophysicists, pp. 1613–1617.

Aminu, M.D., Nabavi, S.A., Rochelle, C.A. & Manovic, V. (2017) A review of developments in carbon dioxide storage. *Applied Energy*, 208, 1389–1419.

Andrés, J., Draganov, D., Schimmel, M., Ayarza, P., Palomeras, I., Ruiz, M., & Carbonell, R. (2019) Lithospheric image of the Central Iberian Zone (Iberian Massif) using global-phase seismic interferometry. *Solid Earth*, 10, 1937–1950.

Bellezza, C., Barison, E., Farina, B., Poletto, F., Meneghini, F., Bohm, G., Draganov, D., Janssen, M., van Otten, G., Stork, A., Chalari, A., Schleifer, A. & Durucan, S. Helically wound cable (HWC) distributed acoustic sensors (DAS) and co-located geophone data: a multi-sensor seismic processing approach in the monitoring of CO$_2$ storage at the Hellisheiði geothermal power plant in Iceland. *Sustainability*. Submitted for publication. Special issue on geological insights for a carbon-free, sustainable environment.

Beyreuther, M., Barsch, R., Krischer, L., Megies, T., Behr, Y. & Wassermann, J. (2010) ObsPy: A Python toolbox for seismology. *Seismological Research Letters*, 81(3), 530–533.

Casas, J., Draganov, D., Badi, G., Manassero, M., Olivera Craig, V., Franco Marín, L., Gómez, M. & Ruigrok, E. (2019) Seismic interferometry applied to local fracture seismicity recorded at Planchón-Peteroa Volcanic Complex, Argentina-Chile. *Journal of South American Earth Sciences*, 92, 134–144.

Claerbout, J.F. (1968) Synthesis of a layered medium from its acoustic transmission response. *Geophysics*, 33(2), 264–269.

Clark, D.E., Oelkers, E.H., Gunnarsson, I., Sigfússon, B., Snæbjörnsdóttir, S.Ó., Aradottir, E.S. & Gíslason, S.R. (2020) Carbfix2: CO$_2$ and H$_2$S mineralization during 3.5 years of continuous injection into basaltic rocks at more than 250°c. *Geochimica et Cosmochimica Acta*, 279, 45–66.

Draganov, D., Campman, X., Thorbecke, J., Verdel, A. & Wapenaar, K. (2010) Event-driven seismic interferometry with ambient seismic noise. In: *72nd EAGE conference and exhibition incorporating SPE EUROPEC 2010*. Houten, the Netherlands: European Association of Geoscientists & Engineers, pp. cp–161.

Duran Neme, J.A. (2021) *Numerical sensitivity kernels in elastic media for imaging purposes and seismic tomography in the Hengill geothermal field*. PhD thesis, ETH Zurich.

Durucan, S., Korre, A., Parlaktuna, M., Senturk, E., Wolf, K.-H., Chalari, A., Stork, A., Nikolov, S., de Kunder, R., Sigfusson, B., Hjörleifsdóttir, V., Andersen, N. & Poletto, F. (2021) SUCCEED: A CO$_2$ storage and utilisation project aimed at mitigating against greenhouse gas emissions from geothermal power production. In: *Proceedings of the 15th greenhouse gas control technologies conference*, 1-7.

Einarsson, P. (2008) Plate boundaries, rifts and transforms in Iceland. *Jökull*, 58(12), 35–58.

Franzson, H., Gunnlaugsson, E., Árnason, K., Sæmundsson, K., Steingrímsson, B. & Harðarson, B. (2010) The Hengill geothermal system, conceptual model and thermal evolution. In: *Proceedings of the World Geothermal Congress*. The Hague: IGA, 1–9.

Furre, A.-K., Eiken, O., Alnes, H., Vevatne, J.N. & Kiær, A.F. (2017) 20 years of monitoring CO$_2$-injection at Sleipner. *Energy Procedia*, 114, 3916–3926.

Gebrehiwot, K., Koestono, H., Franzson, H. & Mortensen, A.K. (2010) Borehole geology and hydrothermal alteration of well HE-24, Hellisheidi geothermal field, SW-Iceland. In: *Proceedings World Geothermal Congress*. The Hague: IGA, 1–9.

Huang, F., Bergmann, P., Juhlin, C., Ivandic, M., Lüth, S., Ivanova, A., Kempka, T., Henninges, J., Sopher, D. & Zhang, F. (2018) The first post-injection seismic monitor survey at the Ketzin pilot CO$_2$ storage

site: results from time-lapse analysis. *Geophysical Prospecting*, 66(1), 62–84.

Jakobsdóttir, S.S. (2008) Seismicity in Iceland: 1994–2007. *Jökull*, 58, 75–100.

Janssen, M., Draganov, D., Bos, J., Farina, B., Barnhoorn, A., Poletto, F., van Otten, G., Wolf, K. & Durucan, S. (2022) Monitoring CO_2 injection into basaltic reservoir formations at the Hellisheiði geothermal site in Iceland: Laboratory experiments. In: *83rd EAGE annual conference & exhibition*, volume 2022. Houten, the Netherlands: European Association of Geoscientists & Engineers, pp. 1–5.

Janssen, M., Russel, J., Barnhoorn, A., Draganov, D., Wolf, K. & Durucan, S. (2020) Seismic velocity characterization and modelling for synergetic utilisation of CO_2 storage coupled with geothermal energy extraction. In: *The first geoscience & engineering in energy transition conference*, volume 2020. Houten, the Netherlands: European Association of Geoscientists & Engineers, pp. 1–6.

Kanakiya, S., Adam, L., Esteban, L., Rowe, M.C. & Shane, P. (2017) Dissolution and secondary mineral precipitation in basalts due to reactions with carbonic acid. *Journal of Geophysical Research: Solid Earth*, 122(6), 4312–4327.

Kim, D., Brown, L.D., Árnason, K., Ágústsson, K. & Blanck, H. (2017) Magma reflection imaging in Krafla, Iceland, using microearthquake sources. *Journal of Geophysical Research: Solid Earth*, 122, 5228–5242.

Krischer, L., Megies, T., Barsch, R., Beyreuther, M., Lecocq, T., Caudron, C. & Wassermann, J. (2015) ObsPy: A bridge for seismology into the scientific Python ecosystem. *Computational Science & Discovery*, 8(1), 014003.

Lumley, D. (2010) 4D seismic monitoring of CO_2 sequestration. *The Leading Edge*, 29(2), 150–155.

Masson-Delmotte, V., Zhai, P., Pörtner, H.-O., Roberts, D., Skea, J., Shukla, P.R., Pirani, A., Moufouma-Okia, W., Péan, C., Pidcock, R., Connors, S., Matthews, J., Chen, Y., Zhou, X., Gomis, M., Lonnoy, E., Maycock, T., Tignor, M. & Waterfield, T. (2018) *Global warming of 1.5 C. An IPCC special report on the impacts of global warming of 1.5˚C above pre-industrial levels and related global greenhouse gas emission pathways, in the context of strengthening the global response to the threat of climate change, sustainable development, and efforts to eradicate poverty*. Cambridge, UK: Cambridge University Press.

Matter, J., Broecker, W., Gislason, S., Gunnlaugsson, E., Oelkers, E., Stute, M., Sigurdardóttir, H., Stefansson, A., Alfreðsson, H., Aradóttir, E., et al. (2011) The CarbFix pilot project - storing carbon dioxide in basalt. *Energy Procedia*, 4, 5579–5585.

Matter, J., Stute, M., Snaebjörnsdottir, S., Oelkers, E., Gislason, S., Aradottir, E., Sigfusson, B., Gunnarsson, I., Sigurdardottir, H., Gunnlaugsson, E., et al,. (2016) Rapid carbon mineralization for permanent disposal of anthropogenic carbon dioxide emissions. *Science*, 352(6291), 1312–1314.

Metz, B., Davidson, O., De Coninck, H., Loos, M., Meyer, L. & Eds. (2005) *IPCC special report on carbon dioxide capture and storage*. Cambridge, UK: Cambridge University PressCambridge University Press.

Nakata, N., Chang, J.P. & Lawrence, J.F. (2015) Body-wave extraction and tomography at Long Beach, CA, with ambient-noise interferometry. *Journal of Geophysical Research: Solid Earth*, 120(2), 1159–1173.

Nakata, N., Snieder, R. & Behm, M. (2014) Body-wave interferometry using regional earthquakes with multidimensional deconvolution

after wavefield decomposition. *Geophysical Journal International*, 199, 1125–1137.

Nishitsuji, Y., Minato, S., Boullenger, B., Gomez, M., Wapenaar, K. & Draganov, D. (2016) Crustal-scale reflection imaging and interpretation by passive seismic interferometry using local earthquakes. *Interpretation*, 4(3), SJ29–SJ53.

Obermann, A., Wu, S.-M., Ágústsdóttir, T., Duran, A., Diehl, T., Sánchez-Pastor, P., Kristjansdóttir, S., Hjörleifsdóttir, V., Wiemer, S. & Hersir, G.P. (2022) Seismicity and 3-D body-wave velocity models across the Hengill geothermal area, SW Iceland. *Frontiers in Earth Science*, 10, 969836.

Olivier, G., Brenguier, F., Campillo, M., Lynch, R. & Roux, P. (2015) Body-wave reconstruction from ambient seismic noise correlations in an underground mine. *Geophysics*, 80(3), KS11–KS25.

Panea, I., Draganov, D., Almagro Vidal, C. & Mocanu, V. (2014) Retrieval of reflections from ambient noise recorded in the Mizil area, Romania. *Geophysics*, 79(3), Q31–Q42.

Pevzner, R., Urosevic, M., Tertyshnikov, K., AlNasser, H., Caspari, E., Correa, J., Daley, T., Dance, T., Freifeld, B., Glubokovskikh, S., et al. (2020) Active surface and borehole seismic monitoring of a small supercritical CO_2 injection into the subsurface: experience from the CO2CRC Otway project. In: *Active geophysical monitoring*. Amsterdam: Elsevier, pp. 497–522.

Polychronopoulou, K., Lois, A. & Draganov, D. (2020) Body-wave passive seismic interferometry revisited: mining exploration using the body waves of local microearthquakes. *Geophysical Prospecting*, 68, 232–253.

Poux, B., Gunnarsdóttir, S.H. & O'Brien, J. (2018) 3-D modeling of the Hellisheiði geothermal field, Iceland, using Leapfrog. *Geothermal Resources Council Transactions*, 42, 524–542.

Ratouis, T.M., Snæbjörnsdóttir, S.Ó., Voigt, M.J., Sigfússon, B., Gunnarsson, G., Aradóttir, E.S. & Hjörleifsdóttir, V. (2022) Carbfix 2: a transport model of long-term CO_2 and H_2S injection into basaltic rocks at Hellisheidi, SW-Iceland. *International Journal of Greenhouse Gas Control*, 114, 103586.

Roy, D.G., Vishal, V. & Singh, T.N. (2016) Effect of carbon dioxide sequestration on the mechanical properties of Deccan basalt. *Environmental Earth Sciences*, 75(9), 1–13.

Ruigrok, E., Campman, X., Draganov, D. & Wapenaar, K. (2010) High-resolution lithospheric imaging with seismic interferometry. *Geophysical Journal International*, 183(1), 339–357.

Ruigrok, E. & Wapenaar, K. (2012) Global-phase seismic interferometry unveils P-wave reflectivity below the Himalayas and Tibet. *Geophysical Research Letters*, 39(L11303), 1–6.

Sigfússon, B., Gislason, S.R., Matter, J.M., Stute, M., Gunnlaugsson, E., Gunnarsson, I., Aradottir, E.S., Sigurdardottir, H., Mesfin, K., Alfredsson, H.A., Wolff-Boensich, D., Arnarsson, M.T. & Oelkers, E.H. (2015) Solving the carbon-dioxide buoyancy challenge: the design and field testing of a dissolved CO_2 injection system. *International Journal of Greenhouse Gas Control*, 37, 213–219.

Sim, C.Y. & Adam, L. (2016) Are changes in time-lapse seismic data due to fluid substitution or rock dissolution? A CO_2 sequestration feasibility study at the Pohokura field, New Zealand. *Geophysical Prospecting*, 64(4-Advances in Rock Physics), 967–986.

Snæbjörnsdóttir, S.Ó., Tómasdóttir, S., Sigfússon, B., Aradóttir, E.S., Gunnarsson, G., Niemi, A., Basirat, F., Dessirier, B., Gislason, S.R., Oelkers, E.H., et al,. (2018) The geology and hydrology of the CarbFix2 site, SW-Iceland. *Energy Procedia*, 146, 146–157.

Snæbjörnsdóttir, S.Ó., Wiese, F., Fridriksson, T., Ármansson, H., Einarsson, G.M. & Gislason, S.R. (2014) CO$_2$ storage potential of basaltic rocks in Iceland and the oceanic ridges. *Energy Procedia*, 63, 4585–4600.

Stoch, A. (2020) *Analysis of seismic data acquired in the Hverahlíd geothermal area*. Master's thesis, Uppsala Universitet, Uppsala.

Stork, A., Poletto, F., Draganov, D., Janssen, M., Hassing, S., Meneghini, F., Böhm, G., David, A., Farina, B., Schleifer, A., Durucan, S., Brynjarsson, B., Hjörleifsdóttir, V., Perry, W., Van Otten, G., Barnhoorn, A., Wolf, K.-H., Korre, A., Bos, J., Bellezza, C., Chalari, A., Obermann, A. & Sánchez-Pasto, P. (2022) Monitoring CO$_2$ injection with passive and active seismic surveys: case study from the Hellisheið i geothermal field, Iceland. In: *Proceedings of the 16th Greenhouse Gas Control Technologies Conference (GHGT-16) Lyon, France.* 1–12.

Verdel, A., Boullenger, B., Martins, J.E., Obermann, A., Toledo, T. & Jousset, P. (2019) Ambient noise seismic reflection interferometry at the Los Humeros geothermal field, Mexico. In: *European Geothermal Congress, Den Haag*. Brussels: EGEC, 1–9.

Verdel, A., Wedemeijer, H., Paap, B., Vandeweijer, V., Weemstra, K., Jousset, P., Franke, S., Blanck, H., Hersir, G., Páll, Verdel, A., Weemstra, V., Paap, B., Weemstra, C., Ágústsson, K. & Hersir, G. (2016) Reykjanes ambient noise reflection interferometry Reykjanes ambient noise reflection interferometry. In: *European Geothermal Congress*, *Strasbourg, France.* Brussels: EGEC, 1–10.

Wapenaar, K., Draganov, D., Snieder, R., Campman, X. & Verdel, A. (2010) Tutorial on seismic interferometry: Part 1 - basic principles and applications. *Geophysics*, 75(5), 195–209.

Wapenaar, K. & Fokkema, J. (2006) Green's functions representations for seismic interferometry. *Geophysics*, 71(4), 33–46.

Wapenaar, K., Thorbecke, J. & Draganov, D. (2004) Relations between reflection and transmission responses of three-dimensional inhomogeneous media. *Geophysical Journal International*, 156, 179–194.